Superconductor Science and Technology

PAPER • **OPEN ACCESS**

Design and characterisation of *ex situ* bulk MgB_2 superconductors containing a nanoscale dispersion of artificial pinning centres

To cite this article: G A B Matthews *et al* 2020 *Supercond. Sci. Technol.* **33** 034006

OPEN ACCESS
IOP Publishing
Made open access 23 September 2020
Superconductor Science and Technology
Supercond. Sci. Technol. **33** (2020) 034006 (11pp)
https://doi.org/10.1088/1361-6668/ab6959

Design and characterisation of *ex situ* bulk MgB_2 superconductors containing a nanoscale dispersion of artificial pinning centres

G A B Matthews, J Liu, C R M Grovenor, P S Grant and S Speller

Materials Department, University of Oxford, Parks Road, OX13PH, Oxford, United Kingdom

E-mail: guillaume.matthews@materials.ox.ac.uk

Received 30 September 2019, revised 18 December 2019
Accepted for publication 8 January 2020
Published 27 January 2020

Abstract

MgB_2 pellets containing a nanoscale dispersion of artificial pinning centres have been successfully manufactured through a powder metallurgy route based on the oxide dispersion strengthened (ODS) concept more usually used for steels and superalloys. Commercial MgB_2 powder and Y_2O_3 nano-powder were mechanically alloyed in a high energy planetary ball mill and consolidated using the field assisted sintering technique. The composite powders were ball milled for different times up to 12 h and characterised by means of particle size analysis, x-ray diffraction (XRD) and scanning transmission electron microscopy (STEM). The microstructure and superconducting properties were characterised by density, XRD, STEM and magnetic property measurements. The powder microstructure comprised Y_2O_3 particles dissolved into the MgB_2 matrix. After consolidation there was a near-uniform dispersion of precipitated YB_4 and MgO particles. A bulk 0.5 wt% Y_2O_3-MgB_2 composite showed the best superconducting performance with a significant improvement in J_c at high field compared with unmodified MgB_2, and only a small reduction in T_c. The results suggest that the ODS concept is promising to improve the superconducting properties of MgB_2.

Keywords: MgB_2, bulk, microstructure, processing

(Some figures may appear in colour only in the online journal)

1. Introduction

Since the discovery of its superconducting properties in 2001 [1] MgB_2 has become a popular and promising material for superconductivity applications due to its interesting combination of properties. The critical temperature (T_c) of 39 K is the highest of any binary compound at ambient pressure, and makes it more suitable for helium-free applications than other low temperature superconductors such as NbTi and Nb_3Sn. In comparison to most high temperature superconducting compounds (HTS), MgB_2 does not contain any rare earth or toxic elements and is much easier to process [2]. Unlike HTS materials, MgB_2 bulks do not need to be processed in single grain (or low misorientation polycrystal) form because the larger coherence length in MgB_2 means that high angle grain boundaries do not act as weak links.

To improve the superconducting properties of MgB_2, carbon doping or the addition of oxide particles to increase the critical current density (J_c) has been used. Carbon doping has led to significant improvements in J_c at high field but also causes a severe reduction in T_c [3, 4]. Simple oxide additions in both *in situ* and *ex situ* processed materials can improve J_c values at high field, but decrease J_c at low field without having a significant effect on T_c [5–9]. Others have reported a decrease in J_c at both high and low fields [10, 11]. The effect of different additions on the superconducting properties of MgB_2 are summarised in table 1.

Most of these studies suggest that J_c improvements at high field is due to the presence of nanoscale pinning centres, although most reports do not show any direct evidence of pinning centres and their characteristics; the decrease in J_c at low field is also usually unexplained.

Table 1. Processing conditions and effect of different additions on the superconducting properties of MgB_2 bulk specimens. The effect on J_c at high and low field is represented by either an increase (↑) or decrease (↓) in J_c relative to unmodified MgB_2, processed under the same conditions [5–11].

Author	Processing conditions	Additions	H_{irr} 20 K (T)	T_c (K)	J_c(<2 T) at 20 K	J_c(>3 T) at 20 K
[5]	*In situ*, 15 min at 900 °C	10 wt% Y_2O_3	5.5	38.3	—	↑
[7]	*In situ*, 30 min at 900 °C	10 wt% SiC + 10 wt% Y_2O_3	5	37	↓	↑
[10]	*Ex situ*, 3 min at 1150 °C	0.5 at% Bi_2O_3	3.6	38	↓	↓
[8]	*Ex situ*, 3 min at 1150 °C	1 at% TeO_2	4.8	37.8	↓	↑
[9]	*Ex situ*, 3 min at 1150 °C	0.5 at% GeO_2	5.1	38	↓	↑
[11]	*In situ*, 30 min at 800 °C	15 wt% TiO_2	4.7	37.5	↓	↑
[6]	*In situ*, 5 min at 1000 °C	0.5 wt% Dy_2O_3	5	37.5	—	↑

This study investigates a new route to manufacture bulk MgB_2 pellets of up to 20 mm diameter, containing a nanoscale dispersion of artificial pinning centres based on the oxide dispersion strengthened (ODS) concept more usually used in steels and superalloys. The aim is to first dissolve Y_2O_3 into the MgB_2 lattice by severe plastic work introduced by mechanical alloying, and second to re-precipitate Y-based nano particles during consolidation using the field assisted sintering technique (FAST), also known as resistive sintering [12] or spark plasma sintering [13]. The microstructure and superconducting properties of the bulks have been carefully characterised to provide a better understanding of the effect of the different microstructural features on J_c and T_c values.

2. Experimental details

Mixtures of pre-synthesised MgB_2 (purity: 99%, Alfa Aesar) and nano Y_2O_3 (20–40 nm, purity: 99.999%, PI KEM Ltd) powders were sealed into stainless steel jars with stainless steel balls under an Ar atmosphere. The total mass of the powder was 10 g with a ball-to-powder ratio of 10:1. Mechanical alloying was conducted in a Fritsch P5 planetary ball mill rotated at 350 rpm in repeating cycles of 10 min of milling followed by a 20 min pause to prevent the powders from overheating. After different milling times (10 min, 1, 3, 6 and 12 h) the powders were recovered in a glove box under Ar.

For consolidation, the composite powders were poured into a 20 mm diameter graphite die lined with graphite paper and gently enclosed between two graphite punches. The powders were then cold compacted using a uni-axial pressure of 30 MPa before being transferred in the die into a Dr Fritsch DSP 507 FAST apparatus. The consolidation chamber was evacuated to 1 mbar and maintained at this pressure during the sintering process. The cold compacted green bodies were heated from room temperature to 1150 °C at a rate of 120 °C min^{-1} then held for 5 min at 1150 °C before cooling down naturally. During the first heating step, the pressure was gradually increased to 50 MPa and then maintained during the high temperature dwell time at 1150 °C, before being progressively released during the final cooling step. The FAST current and voltage passing through the die/punch/green body arrangement was 300–900 A and 0.6–1.2 V respectively.

The powders and FAST disks (20 mm in diameter and 4 mm in thickness) were characterised by several techniques, including x-ray diffraction (XRD), scanning transmission electron microscopy (STEM), powder particle analysis, density measurements and magnetometry. The XRD measurements were performed using a PANalytical Empyrean diffractometer with $Cu_{k\alpha}$ radiation ($\lambda = 0.154$ nm) at 40 kV and 40 mA. The lattice parameter, crystallite size, strain and weight fraction of the different phases present in the samples were estimated from the XRD spectra using Rietveld refinement (PANalytical HighScore Plus software). The weight fraction of the different phases was estimated by using the Hill and Howard method [14], implemented in HighScore Plus. Instrumental broadening of peaks was corrected using a Si standard analysed under the same scan conditions. The STEM analysis was performed in a JEOL 3000F at an accelerating voltage of 300 kV, equipped with a high angle annular dark field (HAADF) detector and an Oxford Instrument EDX detector. STEM specimens were prepared by cutting 3 mm disks from thin slices made from the consolidated pellets. The disks were then mechanically polished to approximately 100 μm before being dimpled and finally thinned to perforation with a Fischione 1010 Ion Mill. The transmission Kikuchi diffraction (TKD) investigations were carried out in a Zeiss Merlin field emission gun (FEG) SEM system operating at 20 kV, equipped with a Bruker e-flash high-resolution electron back scattered diffraction (EBSD) detector and an OPTIMUS TKD head. Particle size analysis was performed using a Malvern Master-Sizer laser diffractometer by dispersing the powder in deionised water. The bulk density of the sintered samples was measured in isopropanol using the Archimede method. Magnetisation measurements were acquired with a quantum design physical property measurement system (PPMS) vibrating sample magnetometer (VSM) on cuboid samples cut from consolidated pellets, with dimensions of approximately $2 \times 2 \times 3$ mm. The critical current density was calculated from the full magnetic hysteresis loops using Bean's model [15].

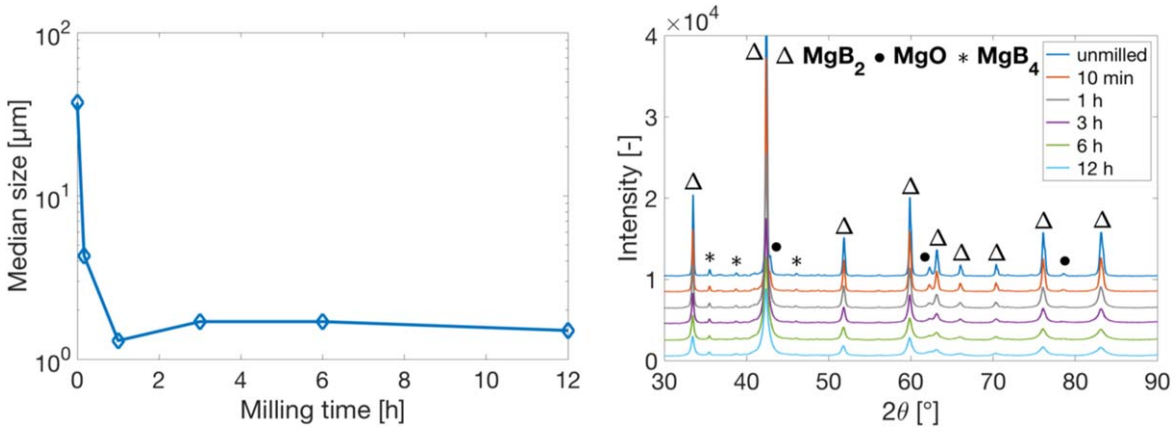

Figure 1. Median size (left) and XRD spectra (right) of the 0.5 wt% Y_2O_3-MgB_2 powders ball milled for different times.

Table 2. Characteristics of the 0.5 wt% Y_2O_3-MgB_2 powder ball milled for different times, estimated using Rietveld refinement.

Milling time	MgO (wt%)	MgB_4 (wt%)	MgB_2 crystallite size (nm)	MgB_2 strain (%)	MgB_2 *a*-axis (Å)	MgB_2 *c*-axis (Å)
0 h	4.7	7	99	0.11	3.0861	3.5242
10 min	5.1	6.9	110	0.13	3.0864	3.5237
1 h	6	7	95	0.23	3.0874	3.5249
3 h	8.1	7.8	81	0.31	3.0873	3.5251
6 h	9.5	9.1	71	0.45	3.0877	3.5266
12 h	10.9	11.1	46	0.52	3.0877	3.5276

3. Results and discussion

3.1. MgB_2 based powders

The median particle diameter of the 0.5 wt% Y_2O_3-MgB_2 composite powder as a function of milling time and their corresponding XRD spectra are shown in figure 1. There was an initial sharp reduction in particle diameter from approximately 40 μm for the pristine powder to 4 μm after only 10 min of milling. The particle diameter then stabilised at 1.5 μm after 1 h of milling, and this is usually interpreted as the point where the rate of fragmentation equals the rate of agglomeration. MgB_2 is intrinsically relatively brittle, leading to the rapid diameter reduction.

The XRD spectra revealed three phases: MgB_2, MgB_4 and MgO. The small fraction of Y_2O_3 added (0.5 wt%) was below the XRD detection limit, hence no Y_2O_3 peaks were observed. MgB_4 and MgO are impurities commonly found in MgB_2 and often present in commercial powders [16, 17]. After milling, the characteristic peaks of all three phases in figure 1 decreased progressively in intensity and became broader, resulting in both an increase in inhomogeneous strain and/or a reduction in effective crystallite size, as shown in table 2. Table 2 summarises the results of Rietveld refinement of the XRD spectra. The pristine powder contained approximately 5 wt% MgO and 7 wt% MgB_4, and the fraction of these impurities increased with milling time. In particular, the MgO fraction increased up to 10.9 wt% after 12 h. Therefore, despite using an Ar filled glove box, it was not possible to fully exclude residual oxygen that reacted with the freshly formed surface of the MgB_2 particles during ball milling. The small increase in MgB_4 fraction was probably a refinement artifact rather than a change in composition. The MgB_4 peaks were relatively weak and difficult to fit during the Rietveld refinement, and the signal to noise ratio decreased with ball milling time which may have led to an overestimation of the total intensity of the MgB_4 peaks relative to the total diffracted intensity.

As commonly seen in mechanically alloyed powders, the crystallite size of MgB_2 decreased and the strain increased with milling time (table 2). Although the refinement of the particle diameter stopped after 1 h of milling, the XRD spectra suggested that refinement of the microstructure (crystallite size) continued. While qualitatively this behaviour is similar to that widely reported for ODS steels, it is perhaps surprising that a brittle compound shows essentially identical trends. Further, there was a gradual increase in the *a* and *c*-axis of the MgB_2 lattice with increasing milling time. Yttrium has a larger atomic size (2.32 Å) than either magnesium or boron (1.73 and 1.92 Å respectively), and the increase in lattice volume may be due to the dissolution (and possible dissociation) of Y_2O_3 into the MgB_2 lattice. Again, similar phenomena are seen in metallic ODS solid solutions at long milling times [18, 19].

The composite powders were further characterized by STEM analysis. High angle annular dark field (HAADF) images of individual powder particles were acquired along with the corresponding Y and O EDX maps. Analysis was conducted on several particles for each milling condition and representative images and EDX maps of powder ball milled for 10 min, 1 and 12 h are shown in figure 2.

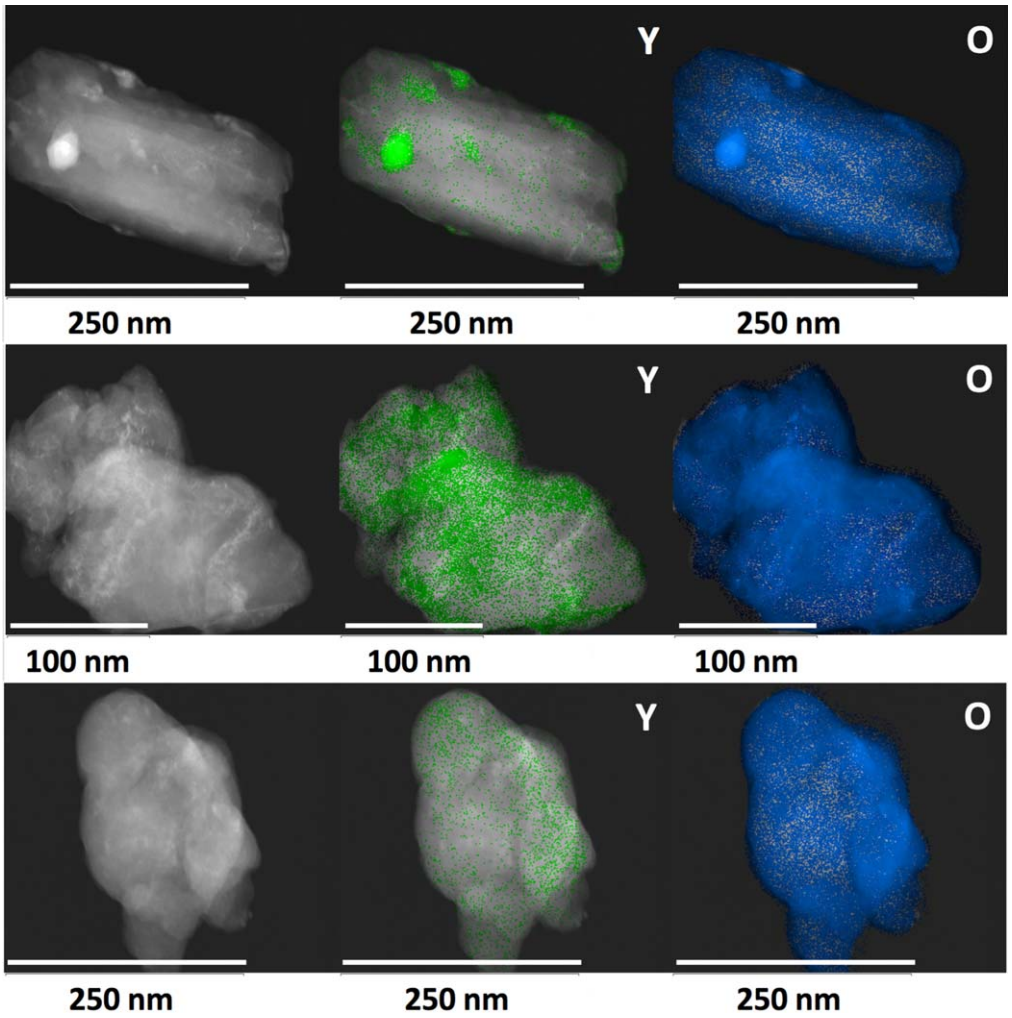

Figure 2. HAADF images, and corresponding Y and O EDX maps of 2 wt% Y_2O_3-MgB_2 powder ball milled for 10 min, 1 and 12 h (top to bottom).

After 10 min of milling, undissolved Y_2O_3 particles of approximately 20–50 nm diameter were embedded in the MgB_2 matrix. The corresponding Y and O maps indicated that Y and O concentrations were co-located. After 1 h of milling, the image contrast was more difficult to interpret due to the high concentration of defects (vacancies and dislocations) introduced by mechanical alloying, and few discrete Y_2O_3 particles could be resolved. Again, in the EDX maps there were areas comparatively richer in both Y and O, but both elements were now more widely dispersed. This trend was confirmed after 12 h of milling where no Y_2O_3 particles could be resolved and the EDX maps showed a much more homogeneous distribution of both Y and O. Consistent with the XRD results above, this suggests that the Y_2O_3 nanoparticles have dissolved into the MgB_2 lattice. In order to further investigate the evolution of the Y_2O_3 phase during the mechanical alloying process, composite powders containing a much higher fraction of Y_2O_3, so that it might be more easily resolved, were fabricated. Figure 3 shows XRD spectra from MgB_2 + 10 wt% Y_2O_3 as a function of milling time.

The initial mix of powders showed a strong (222) Y_2O_3 reflection, which was still visible after 10 min of milling.

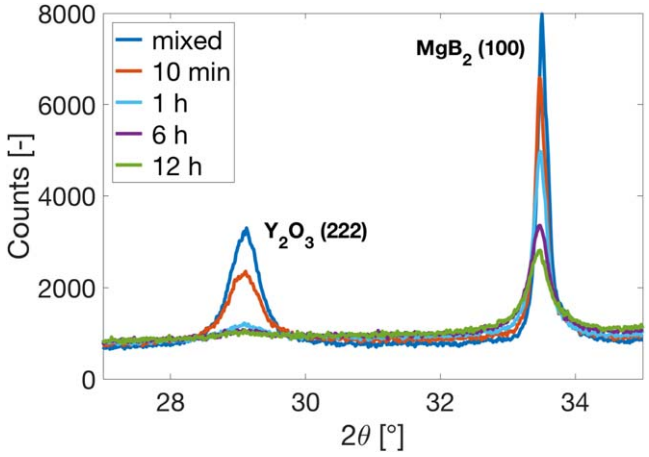

Figure 3. XRD spectra of 10 wt% Y_2O_3-MgB_2 composite powders showing the evolution of the (222) Y_2O_3 and (100) MgB_2 reflections with ball milling time.

However, this peak decreased in intensity after 1 h, and vanished at longer ball milling times. Thus it was concluded that for the composite powders, even when relatively large fractions of Y_2O_3 were added, all the Y_2O_3 was dissolved

Table 3. Composition and processing conditions for MgB_2 based pellets consolidated using the FAST.

Sample	Y_2O_3 (wt%)	Milling time (h)	Temperature (°C)	Dwell time (min)	Pressure (MPa)	Heating rate (°C min^{-1})
MgB_2	0	0	1150	5	50	120
0.5Ym1h	0.5	1	1150	5	50	120
0.5Ym12h	0.5	12	1150	5	50	120
2Ym12h	2	12	1150	5	50	120

Table 4. Density and estimated phase fractions by Rietveld analysis for bulk MgB_2-based pellets consolidated by FAST.

Sample	MgO (wt%)	MgB_4 (wt%)	Relative density (%)	MgB_2 crystallite size (nm)	MgB_2 strain (%)	MgB_2 *a*-axis (Å)	MgB_2 *c*-axis (Å)
MgB_2	8	13	93	151	0.14	3.0838	3.5279
0.5Ym1h	12.5	20.8	90	113	0.16	3.0836	3.5278
0.5Ym12h	15.2	17.3	87	87	0.2	3.0846	3.5287
2Ym12h	14.9	18.7	86	75	0.21	3.0844	3.5281

(presumably as dissociated Y and O) from the EDS maps) into the MgB_2 lattice during mechanical alloying. A further possibility, suggested for some cases of ODS steels, but for which there was no compelling evidence in this particular study, is that the Y_2O_3 becomes first very finely divided and then effectively amorphous (glassy) due to the excessive cold work and ultra-high defect density induced by cold milling [20, 21].

3.2. Bulk MgB_2

The FAST has been successfully used by several research groups to produce dense MgB_2 bulk samples [17, 22, 23]. Dancer *et al* [17] reported that MgB_2 with a relative density of 97% could be obtained by using a temperature of 1250°C and a pressure above 50 MPa. Aldica *et al* [23] achieved densities ranging from 95% to 97% using a temperature of 1150 °C, a pressure of 95 MPa and dwell times between 1 and 20 min. The processing conditions used in this study were chosen based on these findings.

MgB_2-based pellets were manufactured from different Y_2O_3-MgB_2 composite powders and processing conditions summarised in table 3. The three sample codes 0.5Ym1h, 0.5Ym12h and 2Ym12h correspond to bulk pellets manufactured from MgB_2 + 0.5 or 2 wt% Y_2O_3 powders ball milled for 1 or 12 h.

The pellets were first characterized by density measurements and XRD. The bulk density, which includes both open and closed porosity, was measured using the Archimedes method, and the relative density calculated using the estimated phase fractions from the Rietveld refinement. As shown in table 4, longer milling times gave higher MgO fractions. Compared with the powders before consolidation, all consolidated pellets also showed a significant increase in MgB_4 fraction after sintering at 1150 °C. The decomposition reaction $2MgB_2 \rightarrow MgB_4 + Mg_{(g)}$, occurs above 900 °C–1000 °C [24, 25]. The unmodified MgB_2 pellet had the highest relative density of 93% while MgB_2 + Y_2O_3 milled for 1 h had a slightly lower density of 90%, and MgB_2 + Y_2O_3 milled for 12 h had a density below 90%. This suggests that the addition of Y_2O_3 and the increase in MgO fraction due to ball milling had a detrimental effect on densification, perhaps due to the higher intrinsic sintering temperature of MgO [26].

MgB_2 based pellets showed a small increase in MgB_2 crystallite size compared with their respective powders due to coarsening at 1150 °C. Nonetheless, the relatively small crystallite size in the powder milled for 12 h was retained in the bulk samples, and finer than that of unmodified MgB_2. The relatively high temperature consolidation—even for a short time of 5 min—significantly reduced the MgB_2 lattice strain, typically from 0.5% down to 0.2% after sintering.

The consolidated material was again studied by STEM, and typical HAADF images along with Y and O EDX maps of the 0.5Ym1h, 0.5Ym12h and 2Ym12h samples are shown in figure 4. For all the conditions we found relatively fine MgB_2 grains, typically of a diameter of a few hundred nanometres, and numerous MgO and YB_4 nano-particles. As shown in figures 4(c) and (d), fine 20–30 nm MgO particles were within MgB_2 grains, as well as coarser MgO up to 150 nm located at grain boundaries. Figures 4(c) and (d) show that the YB_4 precipitates have a diameter ranging from 20 to 60 nm, and were mainly located at the surface of the larger MgO particles and also within MgB_2 grains. No trace of discrete Y_2O_3 particles was detected. The presence of YB_4 was confirmed by XRD and TKD, as shown in the example given in figure 5 for MgB_2 + 2 wt% Y_2O_3. Song *et al* [5] also found that YB_4 was formed in Y_2O_3 doped MgB_2. In fact, YB_4 can also be synthesised through the borothermal reduction of Y_2O_3 at temperatures around 2000 °C [27]. Although the sintering temperature (here of 1150 °C) was lower, local temperatures in the FAST are known to sometimes be very much higher than the 'bulk' reading from a pyrometer or thermocouple, even if only for a few seconds. In addition, as previously suggested, Y may be dissolved in MgB_2 by milling and may react directly with MgB_2 on re-precipitation to form YB_4. At the same time, dissolved oxygen precipitates as MgO.

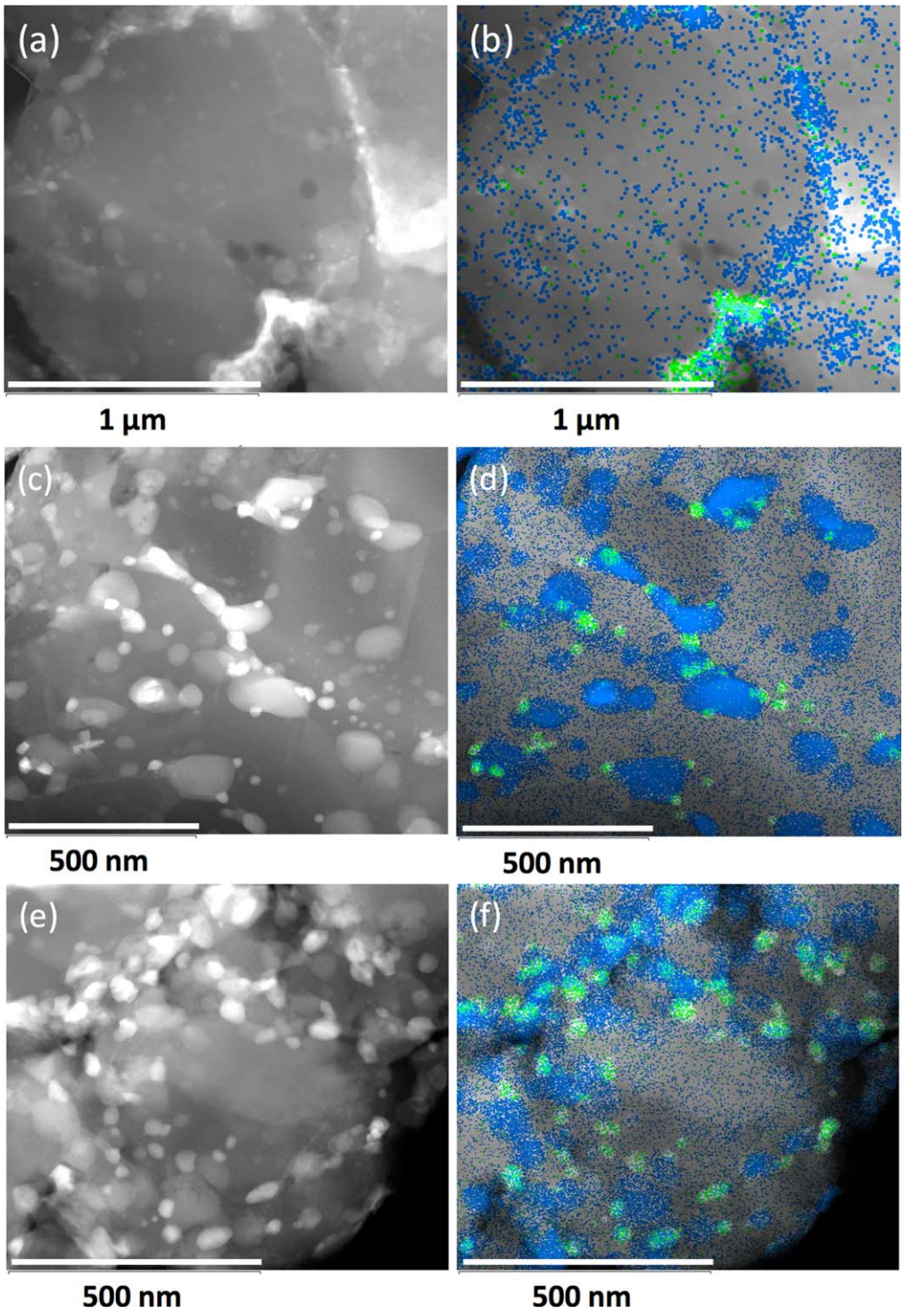

Figure 4. Typical HAADF images and Y (green) and O (blue) EDX maps of specimens (a), (b) 0.5Ym1h, (c), (d) 0.5Ym12h and (e), (f) 2Ym12h.

In a similar study, Mikheenko *et al* [6] also found that fine DyB_4 particles precipitated during resistive sintering of Dy_2O_3 doped MgB_2.

MgB_2 + 0.5 wt% Y_2O_3 after 1 h of milling had a noticeably inhomogeneous YB_4 particle distribution, which mainly formed large agglomerates at grain boundaries, as shown in figures 4(a) and (b). As expected, there was a higher YB_4 fraction in MgB_2 + 2 wt% Y_2O_3 (shown in figures 4(e) and (f)), with most precipitates located at grain boundaries. For MgB_2 + 0.5 wt% Y_2O_3 milled for 12 h the size distributions of the MgO and YB_4 particles are shown in figure 6. The YB_4 particles had a monomodal distribution with most diameters between 20 and 30 nm, and an average diameter of 28 ± 10 nm. XRD spectra of MgB_2 + 10 wt% Y_2O_3 processed under the same conditions gave YB_4 fractions high enough to be detected, and Rietveld analysis gave

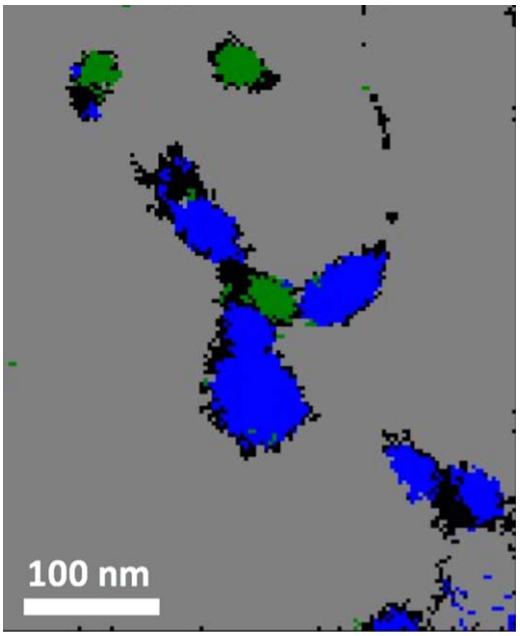

Figure 5. Typical TKD phase map from MgB_2 + 2 wt% Y_2O_3 showing MgB_2 (grey), YB_4 (green) and MgO (blue).

an average diameter of 35 nm, in good agreement with the STEM results. MgO showed a bimodal distribution composed of fine 20–50 nm and coarser 80–120 nm diameters, with an average diameter of 60 ± 30 nm, again similar to the 50 nm extracted from the XRD measurements.

Overall, most of the YB_4 particles nucleated on larger MgO particles, which suggested that MgO was present before YB_4 precipitation, i.e. before sintering. These large MgO particles were probably pre-existing in the as-supplied MgB_2 powder. The finer MgO particles were mainly located inside the MgB_2 grains with a diameter similar to the YB_4 precipitates, which may indicate they were formed and coarsened during the FAST process. This suggests that the addition and dissolution of Y_2O_3 in the MgB_2 matrix during mechanical alloying had the double effect of producing a fine dispersion of both YB_4 and MgO during sintering. This is dissimilar to ODS alloys where predominantly Y_2O_3 is re-precipitated, albeit with more complex transition phases sometimes involved, such as Y–Ti–O phases in Fe–Cr–Ti containing matrices [19].

The superconducting properties of the pellets are shown in figure 7 and summarised in table 5. Figure 7(a) shows the normalised susceptibility curves, with T_c values for unmodified MgB_2, MgB_2 + 0.5 wt% Y_2O_3 milled for 1 h, MgB_2 + 0.5 wt% Y_2O_3 milled for 12 h and MgB_2 + 2 wt% Y_2O_3 milled for 12 h estimated as 38.7, 38.1, 37.7 and 37.2 K respectively. T_c in MgB_2 is well-known to be affected by any deviation from an ideal MgB_2 crystal structure, and is thus sensitive to doping, strain and defect concentrations, and this explains the degradation in T_c in our samples. MgB_2 + 0.5 wt% Y_2O_3 milled for only 1 h showed the smallest T_c reduction, whereas MgB_2 + 2 wt% Y_2O_3 milled for 12 h had the lowest T_c due to the higher strain. Nonetheless, all the pellets had only a small reduction in T_c, indicating that Y_2O_3 does not have as severe an effect on T_c as carbon [4].

At 4.2 K, the high field properties are best represented on a log-scale J_c–B plot, as shown in figure 7(b). Measurements at lower fields were often compromised by excessive flux jumps below 3 T, so this is not shown in the figure. MgB_2 + 0.5 wt% Y_2O_3 milled for 1 h showed no improvement compared with unmodified MgB_2, but by contrast MgB_2 + 0.5 and 2 wt% Y_2O_3 after 12 h milling both showed an appreciable improvement in J_c over the entire field range, with MgB_2 + 0.5 wt% Y_2O_3 (12 h) displaying the best performance. This strong difference in performance can be directly related to the STEM observations. MgB_2 + 0.5 wt% Y_2O_3 (1 h) showed a relatively poor distribution of YB_4 particles, which formed agglomerates that were much larger than the coherence length of MgB_2 (ξ = 5–10 nm [2]). In consequence, these agglomerates could not act as efficient pinning centres to improve J_c. On the contrary, STEM analysis showed that MgB_2 + 0.5 or 2 wt% Y_2O_3 (12 h) had a much more homogeneous dispersion of finer YB_4 precipitates. Figures 4(e) and (f) also showed that for MgB_2 + 2 wt% Y_2O_3 (12 h) many particles were located at grain boundaries which could be detrimental to the grain connectivity and hinder macroscopic supercurrents. The improvement in J_c was probably a trade-off between an increase in pinning centre density and a degradation of grain connectivity. At 4.2 K, MgB_2 + 0.5 wt% Y_2O_3 (12 h) showed a three fold increase in J_c at 5 T and B_{irr} was improved by 1 T compared to unmodified MgB_2.

At 20 K, unmodified MgB_2 showed the highest self-field J_c (J_{c0}) followed by MgB_2 + 0.5 wt% Y_2O_3 (12 h), MgB_2 + 0.5 wt% Y_2O_3 (1 h), while MgB_2 + 2 wt% Y_2O_3 (12 h) had the lowest J_{c0}. Many parameters can influence J_{c0}, including the total superconducting fraction and grain connectivity. All the MgB_2 + Y_2O_3 materials had a lower relative density and an impurity content significantly higher than unmodified MgB_2. The combination of these features controls the total superconducting fraction and explains why the unmodified MgB_2 pellet, which had the highest total superconducting fraction, also showed the highest J_{c0}. Due to their similar density and composition, all the Y_2O_3-containing variants had a similar total superconducting fraction so that differences in J_{c0} may be due to differences in connectivity. For example, the STEM images in figures 4(a)–(f) suggested that MgB_2 + 0.5 wt% Y_2O_3 (12 h) had a better connectivity than both MgB_2 + 0.5 wt% Y_2O_3 (1 h) and MgB_2 + 2 wt% Y_2O_3 (12 h).

Figure 7(c) also shows that at 20 K, J_c at high field followed a similar trend to J_c(4.2 K): MgB_2 + 0.5 wt% Y_2O_3 (12 h) had the best J_c of 8.6×10^7 A m^{-2} with a two fold increase at 3 T and a 0.3 T improvement in B_{irr} compared with unmodified MgB_2.

These results are in good agreement with the studies of Song [5] and Mikheenko [6] who observed similar J_c improvements in Y_2O_3 and Dy_2O_3 doped MgB_2. The authors found that nano-scale YB_4 or DyB_4 particles were formed

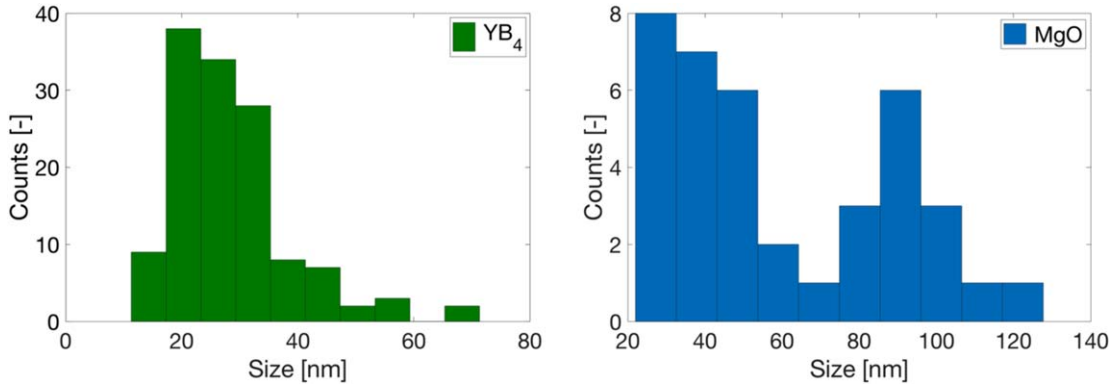

Figure 6. Size distribution of YB_4 and MgO particles found in the 0.5Ym12h specimen.

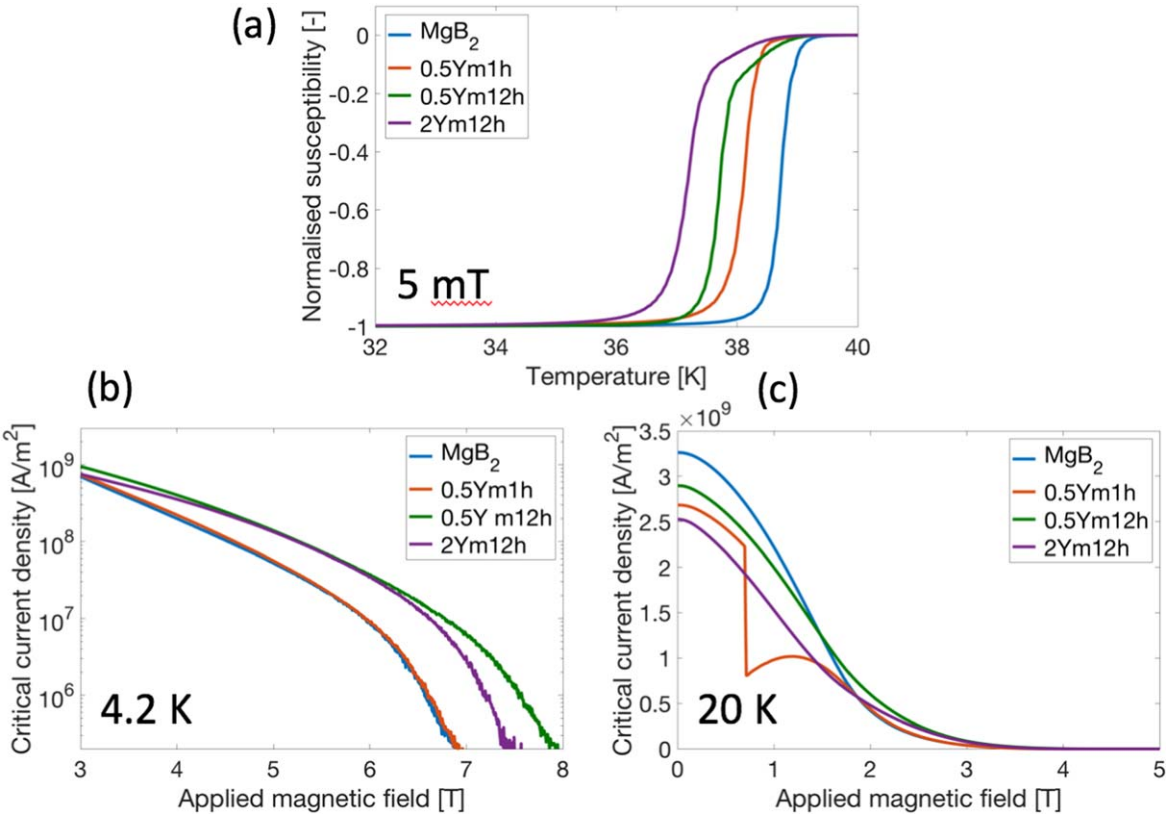

Figure 7. Normalised susceptibility curves of the bulk specimens (a) and J_c–B curves at 4.2 K (b) and 20 K (c). The step observed in the 20 K 0.5Ym1h data is a flux jump.

Table 5. Superconducting properties of the pure MgB_2 and composite bulk specimens.

Sample	T_c (K)	B_{irr} at 4.2 K (T)	J_c at 4.2 K and 5 T (A m^{-2})	B_{irr} at 20 K (T)	J_c at 20 K and 3 T (A m^{-2})
MgB_2	38.7	6.6	5.2×10^7	3.8	4×10^7
0.5Ym1h	38.1	6.6	5.6×10^7	3.8	3.9×10^7
0.5Ym12h	37.7	7.6	14×10^7	4.1	8.6×10^7
2Ym12h	37.2	7.2	13×10^7	4	7.9×10^7

during sintering and acted as efficient pinning centres that enhanced J_c, in particular at high field. They reported higher J_c values than we have obtained in our specimens, but direct comparisons are difficult owing to the fact that both Song and Mikheenko used an *in situ* processing method which tends to lead to higher grain connectivity [28].

To analyse flux pinning mechanisms, the field dependence of the flux pinning force density, $F_p = -J_c \times B$, has been evaluated at 20 K. Figure 8(a) shows the normalised pinning force density, $f_p = \frac{F_p}{F_{pmax}}$, for each sample as a

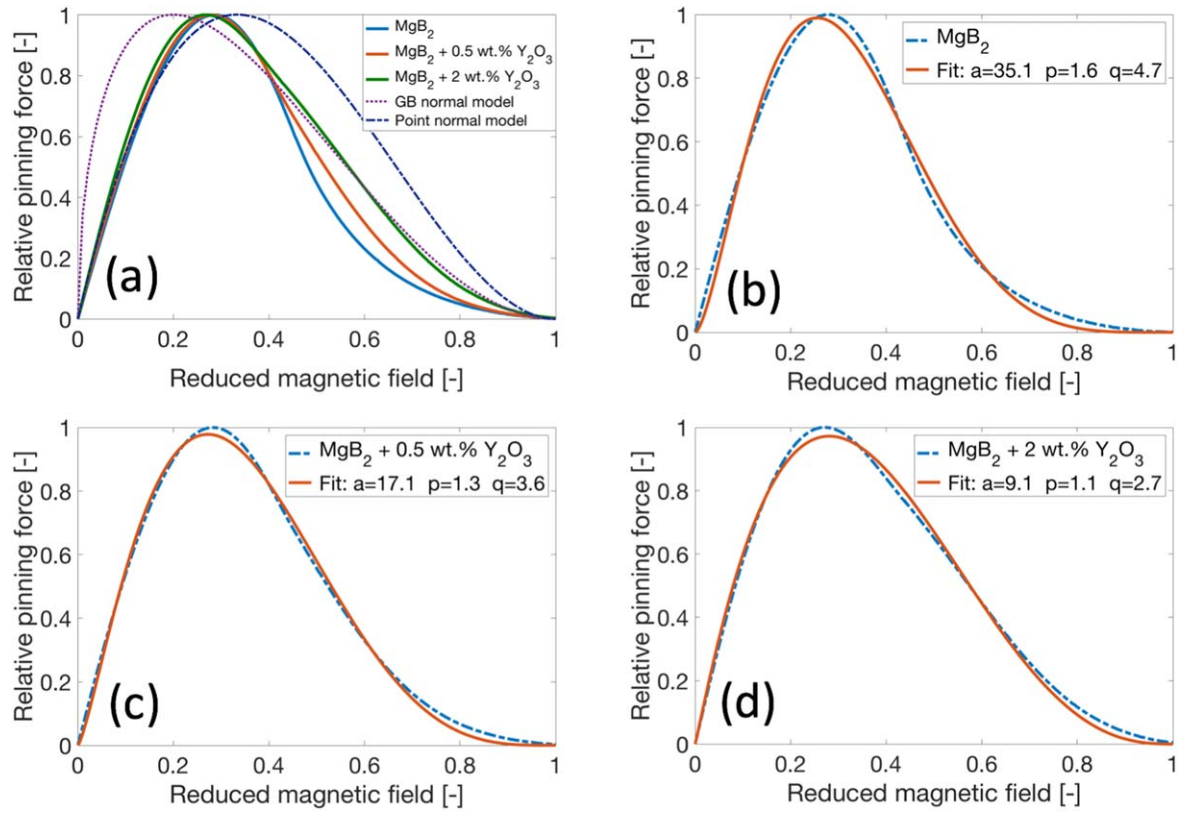

Figure 8. Normalised pinning force curves at 20 K of the bulk specimens (a) Specimens (b)–(d) and theoretical pinning models, (b) unmodified MgB_2, (c) MgB_2 + 0.5 wt% Y_2O_3 (12 h) and (d) MgB_2 + 2 wt% Y_2O_3 (12 h).

function of reduced field, $b = \frac{B}{B^*}$, where B^* is the field where $J_c \rightarrow 0$. The B^* values have been estimated using the method described by Martinez *et al*, which involves linear extrapolation of the low J_c sections of the Kramer curves, $J_c^{\frac{1}{2}} B^{\frac{1}{4}}(B)$, ignoring the zone close to B^* which is known to be strongly affected by flux creep [29]. Theoretical models of flux pinning based on the flux line shear mechanism predict that pinning curves take the functional form $f_p \propto b^p(1-b)^q$, with p and q values depending on the size and shape of the pins relative to the spacing of the flux line lattice and whether the pins are 'normal' material or weaker superconductor with a different Ginzburg Landau parameter ($\Delta\kappa$ pinning) [30].

For polycrystalline MgB_2 bulks, it is expected that the main pinning contributions will come from grain boundaries which give rise to 'surface normal' pinning ($f_p \propto b^{\frac{1}{2}}(1-b)^2$, $b_{peak} = 0.2$) and 'point normal' pinning ($f_p \propto b(1-b)^2$, $b_{peak} = 0.33$) presumably from small non-superconducting inclusions [31]. As can be seen in figure 8(a), the peak in the experimental flux pinning force curves for all three samples is at $b_{peak} \approx 0.25$, which is in between the peak positions expected for ideal 'surface normal' and 'point normal' pinning. This suggests that the pinning mechanisms in all three samples is similar and has contributions from both surface and point pins. However, the shapes of the experimental curves differ from each other and the theoretical curves. In particular, the high field portion of the flux pinning curves, above B_{peak} seems to get broader (and more similar to the theoretical curves) as the amount of Y_2O_3 increases. Figures 8(b)–(d) shows the fits of each experimental curve to a more general function $f_p = ab^p(1-b)^q$. The value of p is reasonably consistent (1.1–1.6), but q is found to increase with reducing doping concentration, with the undoped sample having $q > 4$, much higher than any of the standard models. This has been observed previously in polycrystalline MgB_2 and other superconductors and has been attributed to a wide distribution of superconducting properties (B^*) within the sample [29, 32]. This suggests that the undoped MgB_2 has rather inhomogeneous superconducting properties, and this improves upon doping with Y_2O_3.

In addition, careful inspection of the 2 wt% Y_2O_3 pinning curve shows evidence of a slight shoulder at around 0.5, which may indicate a slight contribution from another pinning mechanism such as 'surface $\Delta\kappa$', which theoretically has a peak at $b_{peak} = 0.6$.

4. Conclusion

Composite Y_2O_3–MgB_2 powders were successfully manufactured by mechanical alloying using high energy ball milling. XRD and STEM suggested that Y_2O_3 slowly dissolved into the MgB_2 matrix during mechanical alloying, by a process of Y_2O_3 dissociation so that Y and O showed a relatively uniform distribution at the nanoscale after 12 h of milling. Milled powders showed significant residual strains up to 0.5% and crystallite sizes of 50–100 nm. Bulk pellets were manufactured using FAST and presented a complex microstructure

composed of a few hundred nanometres MgB_2 grains and a fine dispersion of nanoscale YB_4 and MgO precipitates. After only 1 h of milling, the YB_4 dispersion was relatively inhomogeneous with large agglomerates at grain boundaries, whereas after 12 h of milling YB_4 precipitates were 20 to 40 nm in diameter and more uniformly dispersed.

MgB_2 + 0.5 wt% Y_2O_3 (12 h) showed a significant improvement in J_c(4.2 K) at high field compared with unmodified MgB_2, which was attributed to the relatively fine dispersion of nanoscale YB_4 and MgO precipitates acting as efficient pinning centres. In contrast, MgB_2 + 0.5 wt% Y_2O_3 (1 h) showed no improvement due to a coarser and more inhomogeneous microstructure. MgB_2 + 2 wt% Y_2O_3 (12 h) had poorer superconducting properties, probably due to a reduction in grain connectivity caused by the large fraction of insulating precipitates located at grain boundaries. Adding Y_2O_3 slightly reduced T_c compared with unmodified MgB_2, due to increased strain and defect concentrations that were not fully annealed out at 1150 °C.

The ODS concept was successfully applied to superconductors and has provided a significant improvement in J_c at high field because of the precipitation of a fine dispersion of YB_4 and MgO nano-particles that acted as efficient pinning centres for magnetic vortices. Future work will explore additional processing parameters such as the sintering temperature and time in order to maximise the performance of these ODS superconductors by refining further their nanoscale microstructure.

Acknowledgments

The Authors would like to thank the UK Engineering and Physical Science Research Council and the Department of Materials, University of Oxford for financial support (EP/M508111/1, EP/P026427, Manufacture using Advanced Powder Processes and Process). The Authors acknowledge the use of characterisation facilities within the David Cockayne Centre for Electron Microscopy, Department of Materials, University of Oxford. The data are available at https://doi.org/10.5287/bodleian:Y5Ne86zYJ.

ORCID iDs

J Liu https://orcid.org/0000-0002-9278-6463
S Speller https://orcid.org/0000-0002-6497-5996

References

[1] Nagamatsu J and Nakagawa N 2001 Superconductivity at 39 K in magnesium diboride *Nature* **410** 2–3
[2] Buzea C and Yamashita T 2001 Review of superconducting properties of MgB_2 *Supercond. Sci. Technol.* **14** R115–46
[3] Kim J H *et al* 2012 Microscopic role of carbon on MgB_2 wire for critical current density comparable to NbTi *NPG Asia Mater* **4** e3
[4] Lee S, Masui T and Yamamoto A 2003 Carbon-substituted MgB_2 single crystals *Physica* C **397** 7–13
[5] Song X and Larbalestier D C 2002 High critical current density and improved irreversibility field in bulk MgB_2 made by a scaleable, nanoparticle addition route *Appl. Phys. Lett.* **81** 2026
[6] Mikheenko P, Chen S K and MacManus-Driscoll J L 2007 Minute pinning and doping additions for strong, 20 K, in-field critical current improvement in MgB_2 *Appl. Phys. Lett.* **91** 1–4
[7] Cai Q, Liu Y, Ma Z and Dong Z 2012 Superconducting properties of Y_2O_3/SiC Co-doped bulk MgB_2 *J. Supercond. Novel Magn.* **25** 357–61
[8] Aldica G, Popa S, Enculescu M and Badica P 2012 Enhancement of critical current density and irreversibility field by Te or TeO_2 addition to MgB_2 bulk processed by spark plasma sintering *Scr. Mater.* **66** 570–3
[9] Batalu D, Aldica G, Popa S, Kuncser A, Mihalache V and Badica P 2015 GeO_2-added MgB_2 superconductor obtained by spark plasma sintering *Solid State Sci.* **48** 23–30
[10] Burdusel M, Aldica G, Popa S, Enculescu M, Pasuk I and Badica P 2013 MgB_2 with addition of bi_2O_3 obtained by spark plasma sintering technique *J. Supercond. Novel Magn.* **26** 1553–6
[11] Xu G J 2004 Enhancement of the irreversibility field in bulk MgB_2 by TiO_2 nanoparticle addition *Physica* C **406** 95–9
[12] Mikheenko P, Martinez E and MacManus-Driscoll J L 2007 Grain boundaries and pinning in bulk MgB_2 *Supercond. Sci. Technol.* **20** 264–70
[13] Dancer C E J, Mikheenko P, Bevan A, Abell J S, Todd R I and Grovenor C R M 2009 A study of the sintering behaviour of magnesium diboride *J. Eur. Ceram. Soc.* **29** 1817–24
[14] Hill J and Howard J 1987 Quantitative phase analysis from neutron powder diffraction data using the Rietveld method *J. Appl. Crystallogr.* **20** 467–74
[15] Bean C P 1962 Magnetization of hard superconductors *Phys. Rev. Lett.* **8** 250–3
[16] Kováč P and Grivel J-C 2004 The role of MgO content in *ex situ* MgB_2 wires *Supercond. Sci. Technol.* **17** 41–6
[17] Dancer C E J, Prabhakaran D, Başoğlu M, Yanmaz E, Yan H, Reece M, Todd R I and Grovenor C R M 2009 Fabrication and properties of dense *ex situ* magnesium diboride bulk material synthesized using spark plasma sintering *Supercond. Sci. Technol.* **22** 095003
[18] Zhang L, Ukai S, Hoshino T, Hayashi S and Qu X 2009 Y_2O_3 evolution and dispersion refinement in Co-base ODS alloys *Acta Mater.* **57** 3671–82
[19] Zhang H, Gorley M J, Chong K B, Fitzpatrick M E, Roberts S G and Grant P S 2014 An *in situ* powder neutron diffraction study of nano-precipitate formation during processing of oxide-dispersion-strengthened ferritic steels *J. Alloys Compd.* **582** 769–73
[20] Dai L, Liu Y and Dong Z 2012 Size and structure evolution of yttria in ODS ferritic alloy powder during mechanical milling and subsequent annealing *Powder Technol.* **217** 281–7
[21] Zhao Q, Yu L, Liu Y and Li H 2015 Morphology and structure evolution of Y_2O_3 nanoparticles in ODS steel powders during mechanical alloying and annealing *Adv. Powder Technol.* **26** 1578–82
[22] Lee S Y, Yoo S I, Kim Y W, Hwang N M and Kim D Y 2003 Preparation of dense MgB2 bulk superconductors by spark plasma sintering *J. Am. Ceram. Soc.* **86** 1800–2
[23] Aldica G, Popa S, Enculescu M, Pasuk I, Ionescu A M and Badica P 2018 Dwell time influence on spark plasma-sintered MgB_2 *J. Supercond. Novel Magn.* **31** 317–25
[24] Liu Z-k, Schlom D G, Li Q and Xi X X 2001 Thermodynamics of the Mg-B system: implications for the deposition of films

thermodynamics of the Mg-B system: implications for the deposition of MgB_2 thin films *Appl. Phys. Lett.* **78** 3678

[25] Kario A, Nast R, Häler W, Rodig C, Mickel C, Goldacker W, Holzapfel B and Schultz L 2011 Critical current density enhancement in strongly reactive exsitu MgB_2 bulk and tapes prepared by high energy milling *Supercond. Sci. Technol.* **24** 075011

[26] Gupta T 1971 Sintering of MgO: densification and grain growth *J. Mater. Sci.* **6** 25–32

[27] Zaykoski J A, Opeka M M, Smith L H and Talmy I G 2011 Synthesis and characterization of YB_4 ceramics *J. Am. Ceram. Soc.* **94** 4059–65

[28] Yamamoto A, Tanaka H, Shimoyama J i, Ogino H, Kishio K and Matsushita T 2011 Towards the realization of higher connectivity in MgB_2 conductors: *in situ* or sintered *ex situ*? *Japan. J. Appl. Phys.* **51** 010105

[29] Martínez E, Mikheenko P, Millán A, Bevan A and Abell J S 2007 Flux pinning force in bulk MgB_2 with variable grain size *Phys. Rev.* B **75** 1–8

[30] Dew-Hughes D 1974 Flux pinning mechanisms in type II superconductors *Phil. Mag.* **30** 293–305

[31] Collings E W, Sumption M D, Bhatia M, Susner M A and Bohnenstiehl S D 2008 Prospects for improving the intrinsic and extrinsic properties of magnesium diboride superconducting strands *Supercond. Sci. Technol.* **21** 103001

[32] Wordenweber R 1992 Mechanism of flux-line motion in high-temperature superconductors *Phys. Rev.* B **46** 3076–83